JOURNAL OF MATERIALS SCIENCE **34** (1999) 1711–1719

Boundary characterisation of X65 pipeline steel using analytical electron microscopy

J. Q. WANG*, A. ATRENS, D. R. COUSENS
*Department of Mining, Minerals and Materials Engineering, The University of Queensland, Brisbane, QLD Australia 4072, *State Key Laboratory of Corrosion Science, Institute of Corrosion and Protection of Metals, Chinese Academy of Sciences, Shenyang 110015, P. R. China*
E-mail: atrens@minmet.uq.oz.au

C. NOCKOLDS, S. BULCOCK
Electron Microscopy Unit, University of Sydney, NSW 2006 Australia

Analytical electron microscopy was used to characterise grain boundaries (GBs) and interphase boundaries (IBs) of X65 pipeline steel. There was no segregation of P or S at the proeutectoid ferrite GBs. This indicates that contrary to literature expectations, P and S are unlikely to be involved in the mechanism of SCC of pipeline steels. There was Mn segregation at IBs between pro-eutectoid ferrite and pearlitic cementite, and desegregated from the IBs between pro-eutectoid ferrite and pearlitic ferrite. This pattern of Mn segregation is attributed to diffusion in the process zone ahead of the pearlite during the austenite to pearlite transformation and diffusion in the IBs between the proeutectoid ferrite and pearlite. A new mechanism was proposed for pearlite formation. A GB carbide first forms at an $\alpha : \alpha$ GB, and then grows along the α/γ interface. Subsequently pearlite initiates from this interface carbide. © *1999 Kluwer Academic Publishers*

1. Introduction

The present work was undertaken to characterize the composition of grain boundaries (GBs) and interphase boundaries (IBs) of X65 pipeline steel using an analytical electron microscope (AEM). A GB is the boundary between two grains of the same phase (with the same crystal structure), whereas an IB is the boundary between two different microconstituents or phases. The aim was to contribute to the understanding of intergranular stress corrosion cracking (SCC) as part of our ongoing SCC program [1–15]. The present work also contributes to the understanding of the mechanism of the austenite to pearlite transformation.

Advances in AEM instrument capability allow measurement of localised chemical composition using a probe with a diameter of about 1 nm. This allows testing of the long held hypothesis that preferential corrosion at GBs is the reason for the intergranular crack path during service SCC of pipeline steels. Significant service failures of gas pipelines have been attributed to SCC [16–21]. The chemistry of the intergranular crack path is expected to be formed during steel manufacture, and is widely believed to be related to the chemical segregation of species such as S, P or C [22–24], or related to precipitates, in particular carbides [18]. Alternatively, the grain boundary structure may be intrinsically more prone to corrosion. Our prior work [25, 26] on a X52 pipeline steel using AEM found no S or P segregation but did find Mn segregation, which was related to the thermal history of the steel during steel production, and in particular to the austenite to pearlite transformation. Similar Mn segregation was observed in the present study in X65 pipeline steel and an analysis of this segregation helps to understand the mechanism of pearlite formation in this hypoeutectoid steel.

The study of the transformation from austenite (γ) to pearlite is an age-old topic but is still relevant today as there is increasing pressure on steel technology, particularly for high performance at low cost. The traditional mechanism [27, 28] is for a hemispherical pearlite nodule to be nucleated at a boundary as shown in Fig. 1a. For a hypoeutectoid steel such as the steels under study, it is thought that perlitic ferrite (α_p) is nucleated first, followed by nucleation of pearlitic cementite, C_p, on both sides of the α_p. Subsequently, α_p is nucleated on the sides of the C_p etc and this process is usually described as sideways nucleation. Each platelet of the pearlite nodule (i.e. both the α_p and C_p) also grows in length and this is usually described as edgeways growth of the pearlite. The pearlite grows until separate pearlite colonies impinge on each other, impinge onto existing ferrite or until there is no more austentite to transform.

Cahn and Hagel [29], in a theoretical approach, pointed out that not all grain boundary nucleation sites are equivalent, that the grain corners would be more effective than edges, and that the edges would be better than grain surfaces. This was substantiated experimentally by Mintz [30, 31] who observed that for a C-Mn steel, carbide often initiated at the α/α GBs (i.e. the GBs between proeutectoid grains) to form the tails of pearlite colonies and probably to initiate the pearlite reaction as illustrated in Fig. 1b.

0022–2461 © *1999 Kluwer Academic Publishers*

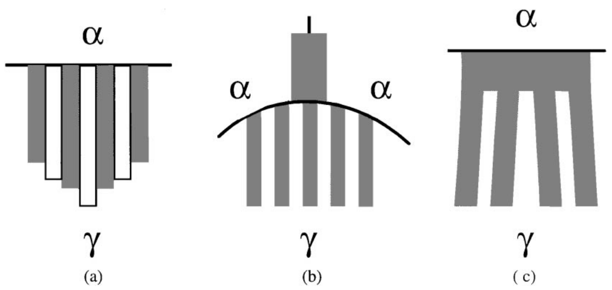

Figure 1 Mechanisms of pearlite formation (a) traditional mechanism of nucleation at $\alpha:\gamma$ IB; (b) mechanism of pearlite formation from carbide at $\alpha:\alpha$ GB; (c) mechanism of pearlite formation from carbide that first forms at $\alpha:\gamma$ interface.

A third mechanism for the pearlite formation was proposed by Ming and Kelly [32, 33] based on experimental observations using a Fe-0.46C-0.65Mn hypoeutectoid steel. Their mechanism proposes that, as the austenite (γ) transforms to ferrite (α), carbon is rejected from the ferrite and consequently the carbon concentration builds up at the α/γ interface until a GB carbide forms at the interface of the ferrite and austenite. Subsequently, pearlite grows from this GB carbide as illustrated in Fig. 1c.

2. Experimental

2.1. TEM sample preparation

The material studied was X65 pipeline steel from a production pipeline. Such steels are typically hot rolled whilst austenitic followed by relatively rapid cooling [34] which leads to their microstructure of proeutectoid ferrite (α) plus pearlite as illustrated in Fig. 2. The pearlite contains ferrite (designated as α_p to distinguish it from proeutectoid ferrite α) and carbide C_p. The chemical composition (in wt %) was 0.07% C, 1.36% Mn, 0.19% Si, 0.002% S, 0.013% P, 0.01% Ni, 0.2% Cr, 0.04% Nb, 0.011% Al and balance Fe.

The present work characterized the grain boundary composition using an analytical electron microscope (AEM). The instrument used was the VG HB601, located at Sydney University (SU). This instrument is a dedicated AEM with a field emmission gun and is a scanning transmission electron microscope. The VG HB601 needs an ultra-high vacuum with gun chamber at 4×10^{-11} mbar. The electron accelerating voltage was 100 kV. Before the analysis the sample was baked in the specimen chamber for 15 min in order to minimize contamination. Sample preparation and preliminary TEM observations with a JOEL 2010 were carried out at The University of Queensland (UQ).

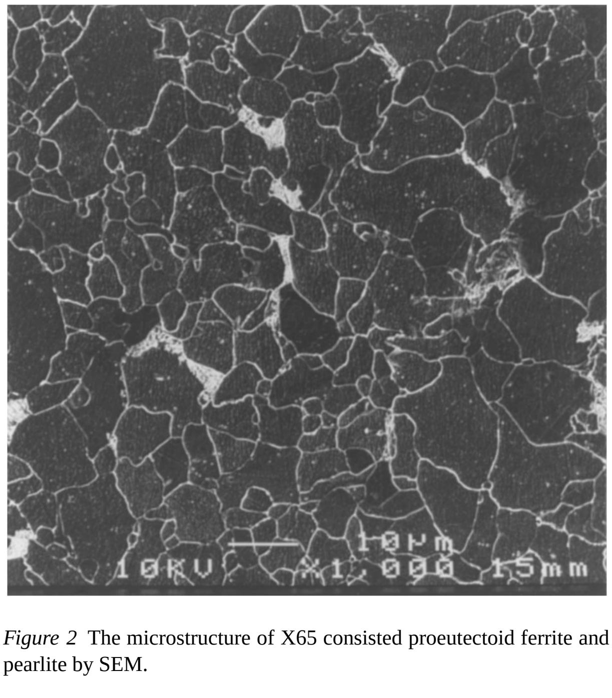

Figure 2 The microstructure of X65 consisted proeutectoid ferrite and pearlite by SEM.

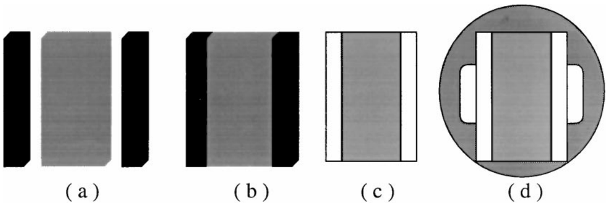

Figure 3 Procedure of TEM sampel preparation (a) cutting one $1\times1\times2$ mm steel, and two $0.5\times1\times2$ mm silicon pieces, (b) sticking steel in the middle of two silicon pieces using M-bond cured at 180 °C for 1 hr; (c) polishing to about 1 μm by using Tripod and diamond papers from 30 μm to 0.1 μm; (d) sticking on the copper grid by using M-bond and then ion milling.

In order to have acceptable EDS signal to noise values from the GB segregation and to minimize the amount of ferromagnetic steel in the AEM, very thin cross-section TEM samples were prepared. The procedure of sample preparation is illustrated in Fig. 3. Small pieces of steel $1\times1\times2$ mm were cut using a slow speed saw. A small sandwich was made by sticking a slice of the steel between two thin (0.5 mm) silicon plates using M-bond 610 adhesive. The small sandwich was stuck onto the ceramic leg of the polishing tripod using “crystal bond” adhesive. This tripod [35] enables the sample to be polished very smooth and very thin. The tripod has three legs, two with micrometers, and one ceramic leg. The sample was stuck onto the ceramic leg, and the two micrometers were adjusted so that the bottoms of the three legs were on one plane. One surface of the small sandwich, which is silicon-steel-silicon, was polished using diamond papers from 30 to 0.1 μm. The sandwich was removed from tripod by heating to remove the “crystal bond” adhesive. The smooth side was stuck onto the tripod using “Super Glue”, and the other side was polished using the diamond papers until the silicon on either side of the steel was a red color which indicates a thickness of about $\sim$2 μm. The sandwich was stuck onto a copper electron-microcopy support grid using M bond. After curing at 180 °C for 1 h, the sample was removed from the ceramic rod of the tripod by dissolving the super glue using acetone and the sample was thinned by ion milling. Between sample preparation and electron microscopy examination, the sample was stored in a vacuum chamber. Before examination in the AEM, the sample was cleaned using plasma etching in a gas mixture of argon at 60 V for 10 min.

2.2. Thickness measurement using convergent beam diffraction (CBD)

The thickness of the TEM specimen was measured using convergent beam diffraction (CBD) [36] using the JEOL 2010 TEM at UQ with an accelerating voltage

200 kV. Thickness measurement was carried out at two typical sites in the thin area of the specimen using CBD. Low magnification photos were taken in order to find the same GBs in the VG601.

The sample was tilted until there were two-beam conditions with only one strongly excited *hkl* reflection. The fringes in the two convergent beam diffraction discs contain the thickness information. The central bright fringe in the diffracted disc is at the exact Bragg condition where the deviation $s = 0$. The fringe spacings in the diffracted disc correspond to the angles $\Delta\theta_i$. From these spacings the deviation s_i can be obtained for the ith fringe from Equation 1:

$$s_i = \lambda \frac{\Delta\theta_i}{2\theta_B d^2} \tag{1}$$

where θ_B is the Bragg angle for the diffracting *hkl* plane, λ is the electron wavelength, d is the *hkl* interplanar spacing, $\Delta\theta_i$ is fringe spacing between central bright fringe and the ith dark fringe on the *hkl* disc. The angle $2\theta_B$ was measured as the distance between the two discs measured using their central fringes. If the extinction distance ξ_g is known, then the foil thickness t can be calculated from Equation 2:

$$\frac{s_i^2}{n_i^2} + \frac{1}{\xi_g^2 n_i^2} = \frac{1}{t^2} \tag{2}$$

where n is an integer. If the extinction distance ξ_g is not known, a graphical method is used, plotting the measurement for several fringes as follows: (1) Assign $n_1 = 1$ for the first fringe, $n_2 = 2$ for the second fringe, etc. and plot $(s_i/n_i)^2$ against $(1/n_i)^2$. (2) If a curve results, then repeat the procedure by re-assigning $n_1 = 2, 3, 4, \ldots$ to the first fringe until a straight line is obtained. (3) The intercept of the straight line is t^{-2}, and the slope is $-\xi_g^{-2}$.

2.3. Thickness measurement by EELS

In-situ measurement of the sample thickness was carried out using electron energy loss spectroscopy (EELS) in the VG HB601 at SU. The thickness was estimated from the low energy region. In this region the intensity is very high. The measurement is rapid and involves only a small electron dose to the specimen. The thickness was calculated from the Equation 3:

$$t = \lambda \ln(I_t/I_0) \tag{3}$$

where I_0 is the zero-loss intensity, I_t is the total intensity reaching the spectrometer measured up to some suitable energy loss Δ, t is the sample thickness, and λ is a mean free path for energy losses less than Δ. The thickness t can be measured if λ is known. λ values for iron and carbon are about 80 and 120 nm, respectively.

2.4. Concentration analysis by EDS

Chemical characterisation was carried out using Energy Dispersive X-Ray Spectroscopy (EDS). The probe size for EDS was about 1 nm, so high resolution analysis was possible. For each analysis, the counting time was 200 s, and over 1,000,000 counts were collected. The quantification method used Cliff-Lorimer ratios [37] with corrections for specimen absorption calculated from a user specified sample density and thickness, normally specified from an EELS measurement of the sample thickness. The absorption corrections used assumes normal incidence of the beam and no tilting of the sample. These conditions were appropriate for all measurements taken in the VG HB601. The Cliff-Lorimer k_{AB} factors used in the analyses were those supplied with the Link ISIS EDS spectrometer and calculated for the HB601 at 100 kV.

Nearly 20 boundaries were analyzed. These included grain boundaries, GBs and interphase boundaries (IBs). A GB is the boundary between two grains of the same phase (with the same crystal structure), whereas an IB is the boundary between two different phases. There were three kinds of boundaries: (1) $\alpha:\alpha$ GBs were the GBs between proeutectoid ferrite grains, (2) $\alpha:\alpha_p$ IBs were the IBs between pro-eutectoid ferrite and pearlitic ferrite, and (3) $\alpha:C_p$ IBs were the IBs between proeutectoid ferrite and pearlitic cementite. The composition was measured across all three types of boundaries. Compositional profiles were also measured across and along various carbides.

3. Results

3.1. Microstructure

The microstructure of the X65 pipeline steel consisted of proeutectoid ferrite, α, plus pearlite as illustrated in Fig. 2, which is a SEM micrograph. At higher magnifications in the TEM, the typical α/α GB appears sharp with no carbides present at the GB. Figure 4a shows a typical IB between pro-eutectoid ferrite and pearlite which in most cases was a gently undulating line which separated the two microstructural constituents. It was a clean boundary with little observable structure at moderate magnifications. However Fig. 4b shows an extremely interesting case, which suggests a new mechanism of pearlite nucleation as illustrated in Fig. 4c. There was a GB carbide (GBC_f) between two α grains. The carbide GBC_f widened gradually from a small nucleus. This GB carbide was very close to an IB carbide (IBC_{fp}) at the interface between proeutectoid ferrite and pearlite. Furthermore, pearlite radiated out from the IB carbide IBC_{fp}.

3.2. Foil thickness measurement

The foil thickness was measured using CBD under two-beam conditions with only one strongly excited *hkl* reflection as shown in Fig. 5. The *022* plane was strongly excited. So the interplanar spacing d was 0.101 nm. The electron wavelength λ was 0.0025 nm at the 200 kV accelerating voltage. The thickness was calculated from the distance between the fringes. The graphical method was used as shown in Fig. 6. The intercept of the straight line is t^{-2}, which indicates that the foil thickness was about 52 nm.

In-situ foil thickness measurements were performed using EELS in the VG HB601. The measured thickness

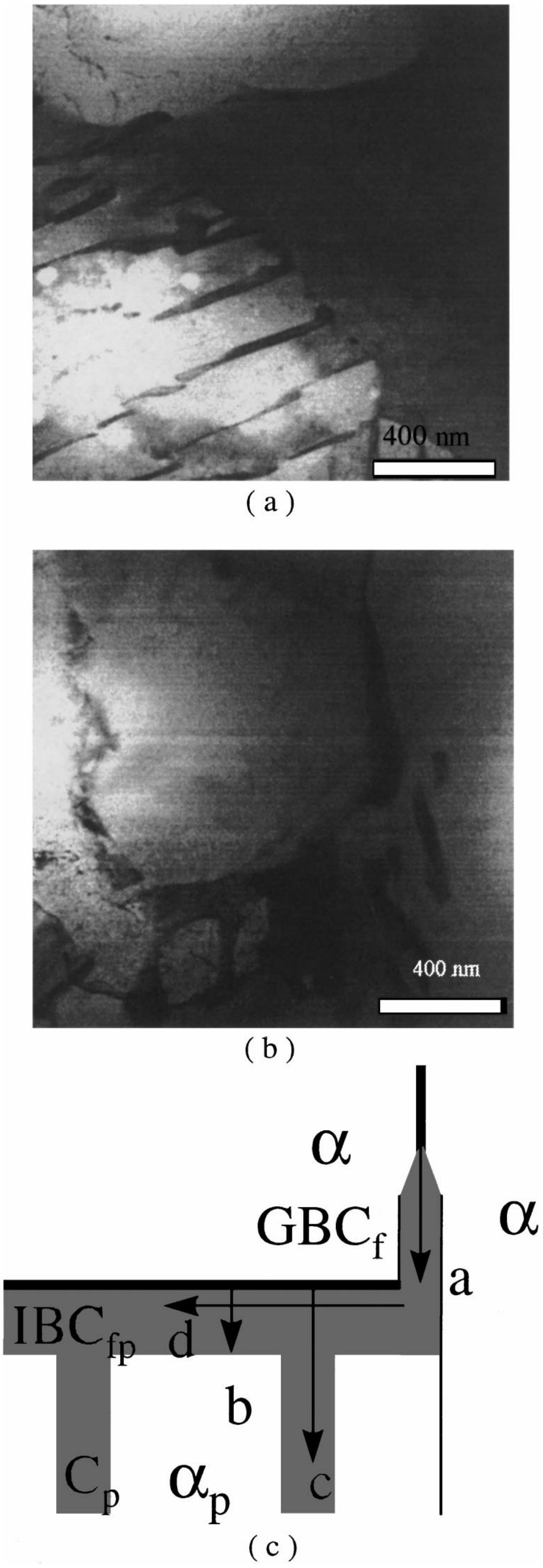

Figure 4 STEM micrograph showing the microstructure of X65 consisting of ferrite and pearlite by STEM. a: boundary between ferrite and pearlite; b: boundary carbide nucleating pearlite c: schematic of new mechanism of pearlite nucleation.

values are listed in Table I. This thickness t includes the carbon contamination film on the sample surface, so it is somewhat larger than the actual foil thickness. The thickness measurement by EELS is a convenient and rapid method which was used to determines appropriate sites for EDS measurements.

TABLE I Thickness of sample and contamination film as measured by EELS

GB#	t (nm)					t av (nm)
x65gb4	46	48	54	66	60	54.8
x65gb8	66	78	56	67	63	66
x65gb16	50	30	30	36	54	40
x65gb17	66	60	54	72	72	64.8
x65gb22	40	39	50	30	36	33

3.3. EDS analysis

A typical EDS spectrum is shown in Fig. 7. There was a significant carbon peak which is attributed to a surface contamination film formed during specimen preparation and transport, particularly during ion milling. Very small peaks due to Cl and Ar (not visible at the scale of Fig. 7) are attributed to the same cause. The Cu peak is expected to have been sputtered from the copper support grid during ion beam thinning. Some Cr and Ni signals are expected from the stainless steel used as a construction material for the vacuum chamber of the VG 601, and the small peak height values are consistent with such a signal source. The O peak was attributed to either surface oxidation of the specimen or could be from the M-bond curing in the oven. P and S have been previously linked to intergranular SCC of steels. In our test, there was no systematic P and S segregation. However, there was Mn segregation to GBs as reported below.

3.3.1. GBs between pro-eutectoid ferrite grains

The Mn profile across α/α GBs is shown in Fig. 8. There was some Mn segregation at this kind of GB.

3.3.2. IBs between pro-eutectoid ferrite and pearlite grains

A typical IB between pro-eutectoid ferrite and pearlite is shown in Fig. 4a. Mn profiles across α/α_p IBs and α/C_p IBs are shown in Figs. 9 and 10, respectively. The Mn concentration inside the α_p was close to that in α, and both were close to the bulk value as listed in Table II. At α/α_p IBs, there was Mn desegregation for a region about 25 nm on each side of the IB. At α/C_p IBs, Mn segregated most significantly on the side of the cementite, and the segregation region was about 20 nm in extent. The Mn concentration decreased with increasing distance from the IB to inside the cementite, but

TABLE II Concentrations of X65 at boundaries and inside grains

	Mn
α	1.18 ± 0.16
α/α	1.53 ± 0.40
α/α_p	0.82 ± 0.25
α/C_p	2.9 ± 0.52
α_p	1.30 ± 0.15
C_p	2.2 ± 0.38
$\alpha_\mathrm{p}/C_\mathrm{p}$	1.35 ± 0.28
bulk	1.36

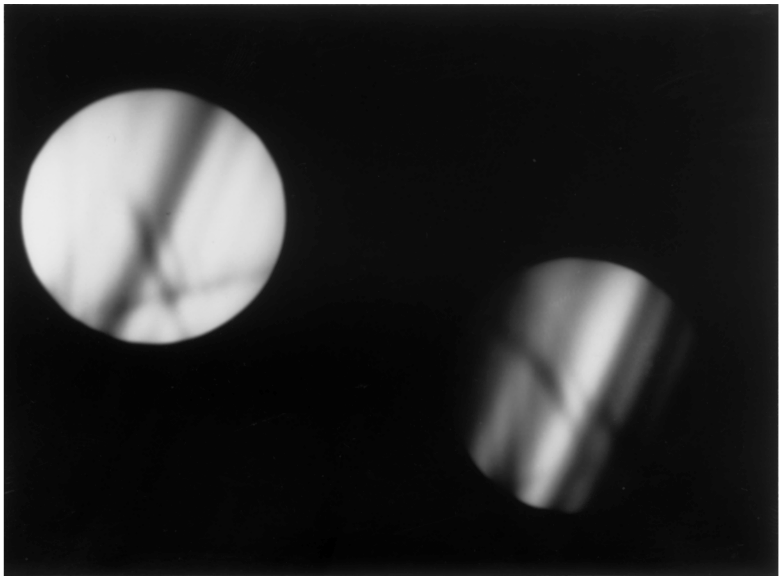

Figure 5 K-M fringes in a ZOLZ CBD pattern from α-Fe taken under two beam conditions with 022 strongly excited.

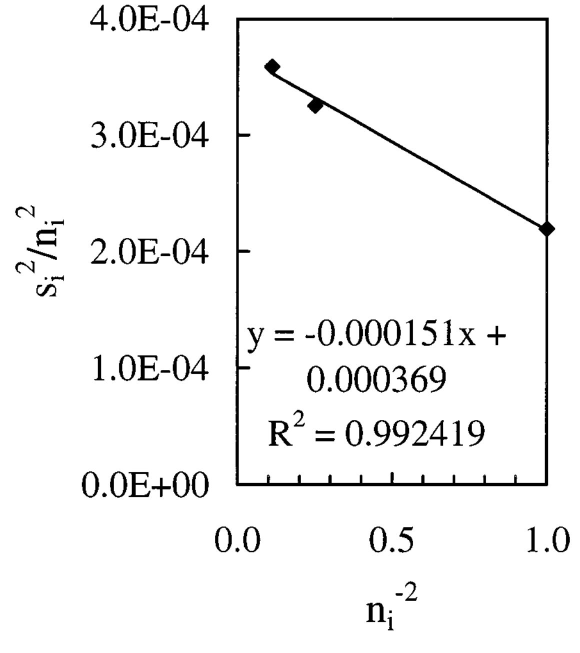

Figure 6 Plot of $(s_i/n_i)^2$ and n_i^{-2}.

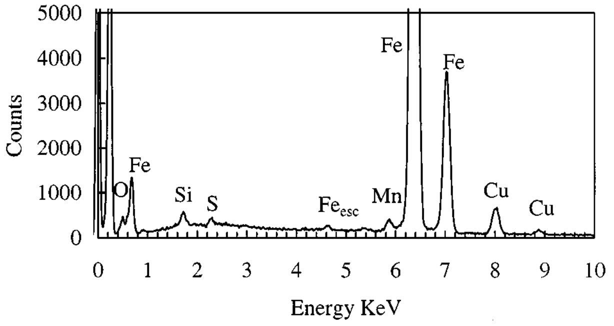

Figure 7 EDS spectrum of X65 TEM sample.

it was still larger than that in the pro-eutectoid ferrite. The cementite was Mn rich.

3.3.3. GB carbide

Fig. 11 shows the Mn profile along the α/α GB carbide GBC_f in the direction 'a' as illustrated in Fig. 4c.

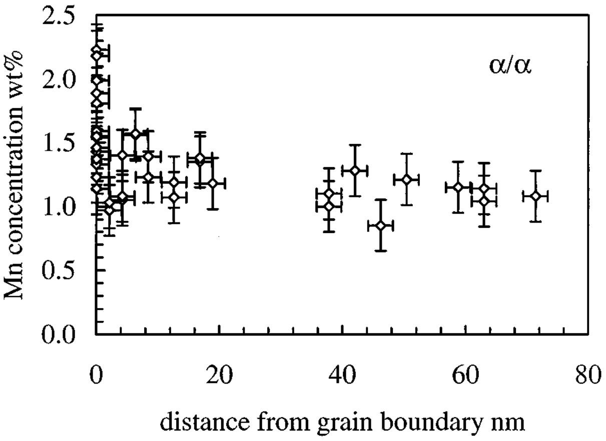

Figure 8 Mn profile across α/α GBs.

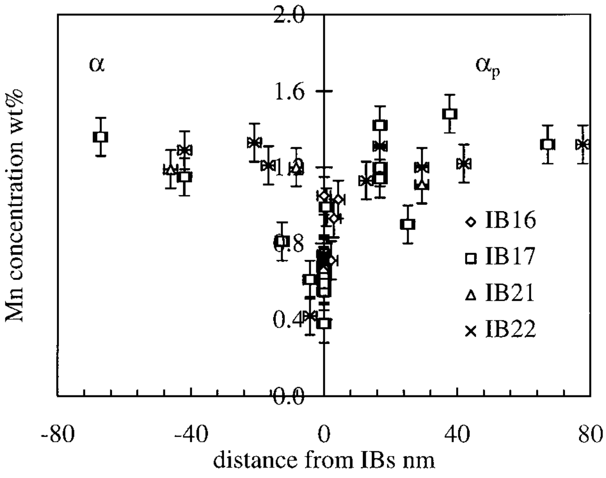

Figure 9 Mn profile across α/α_p IBs.

The GBC_f was Mn rich, but did not grow from a nucleus with a high Mn concentration. Fig. 12 shows that, across IBC_{fp} in the direction 'b' in Fig. 4c, the measured Mn concentration was high in the middle of IBC_{fp}, and low at the boundaries, i.e. low at the α/IBC_{fp} and IBC_{fp}/α_p GBs. Fig. 13 shows the Mn profile across the carbide IBC_{fp} and pearlitic carbide in the direction

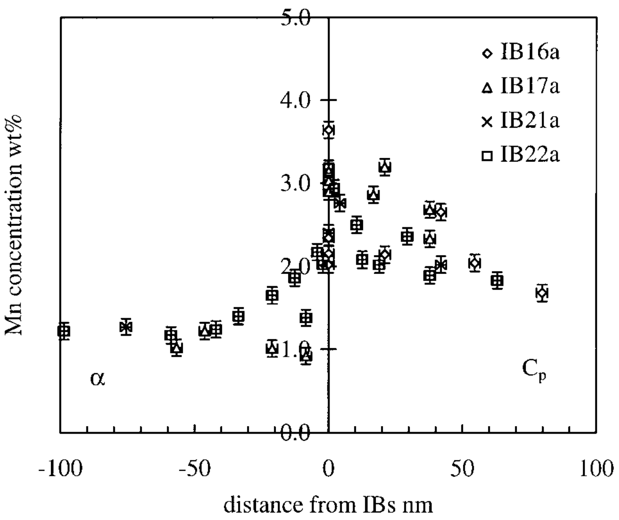

Figure 10 Mn profile across α/C_p IBs.

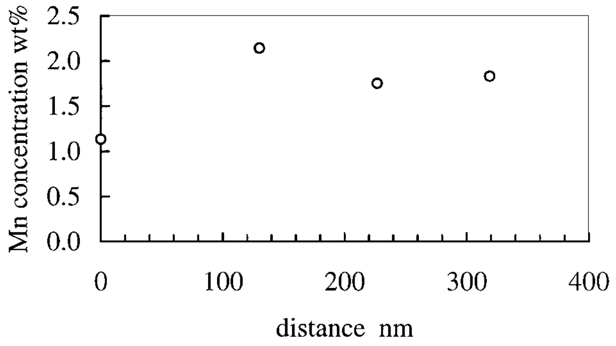

Figure 11 Mn profile along GBC_p in direction 'a' in Fig. 4(c).

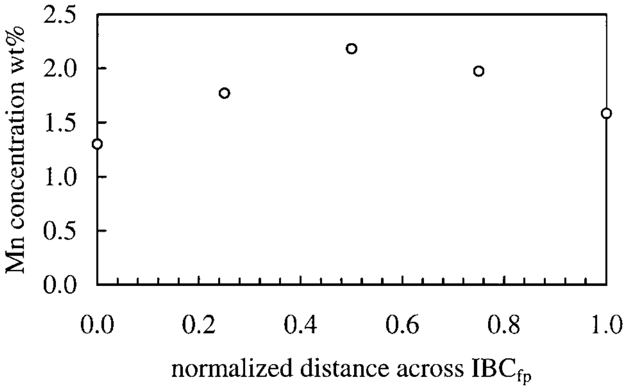

Figure 12 Mn profile along IBC_{fp} in direction 'b'.

'c' in Fig. 4c. Across the IBC_{fp} part, the Mn profile was the same as that in Fig. 12. Along the pearlitic carbide, the Mn increased gradually.

4. Discussion

4.1. Segregation at proeutectoid ferrite GBs

Only some Mn segregation was measured in this work at the proeutectoid ferrite GBs. This is a significant experimental observation in view of the hypothesis that preferential corrosion of the GBs is the reason for the intergranular crack path during service SCC of pipeline steels. Examination of the microstructure of

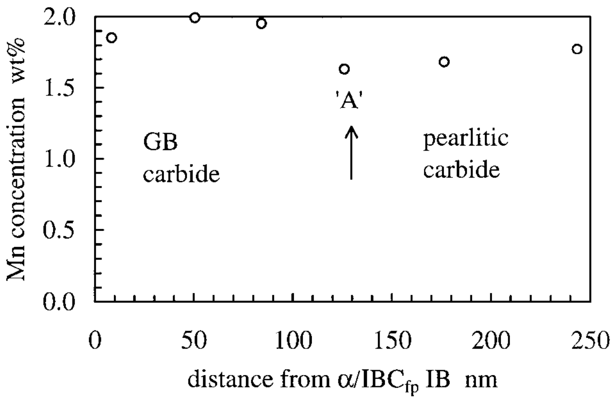

Figure 13 Mn profile across IBC_{fp} and pearlitic carbide along the direction 'c' in Fig. 4(c).

X52 pipeline steel, Fig. 2, indicates that the only continuous microstructural path that proceeds right through the microstructure is a path along the proeutectoid GBs. But, only Mn was measure to segregate at these proeutectoid GBs.

Significant Mn segregation was measured at other boundaries. There was Mn segregation at α/α_p IBs (Fig. 9) and at α/C_p IBs (Fig. 10). Thus the measured Mn segregation strengthens the position that there was indeed no segregation at the proeutectoid ferrite GBs of P and S. This indicates that contrary to literature expectations, P and S are not involved in the mechanism of SCC of pipeline steels.

However, it cannot be concluded that there is no segregation at the proeutectoid ferrite GBs, because there was some Mn segregation and it was not possible to make measurements of carbon concentrations. Moreover, Parkins [18] and Mazille and Uhlig [44] have argued strongly for the role of carbon at GBs in the SCC of alloy steels. This clearly indicates the need for improved specimen preparation procedures to enable the production of AEM samples free of surface carbon contamination. Such procedures exist for cleaning stainless steel and ceramic oxide samples, but the use of these techniques led to the oxidation of the X52 steel samples. Work is currently underway [43] on these cleaning procedures (involving Ar + O plasmas).

4.2. GB carbide

Pearlite formation for hypoeutectoid steel has been studied by many researchers [27–33]. As illustrated in Fig. 1a, the traditional mechanism for pearlite formation is that the pearlite forms at a clean ferrite boundary by edgeways growth and sideways nucleation [27, 28]. The microstructures of pearlite in hypoeutectoid steel observed in two dimensions by TEM and SEM usually seems to agree with this mechanism. The pearlite colonies often do impinge on clean ferrite boundaries.

However, Mintz *et al.* [31] observed carbides at α/α GBs in ferrite-pearlite steels. These GB carbides joined pearlite colonies at triple points, where two ferrite grains met a pearlite colony, as illustrated in Fig. 1b. It is probable that these GB carbides nucleated the pearlite reaction.

Ming [32, 33] carried out a detailed study of the pearlite microstructure and crystallography. They observed that all cementite lamellae in pearlite in hypoeutectoid steel grew from a thin film of cementite at the proeutectoid ferrite IB. They found that all the cementite lamellae in a pearlite colony had the same orientation. However, the crystallography of the cementite film was not related to that of the proeutectoid ferrite. Furthermore, the crystallography of both the cementite and the ferrite lamellae in the pearlite was not related to that of the proeutectoid ferrite. To explain their observations, they proposed (see Fig. 1c) that the thin film of cementite at the proeutectoid ferrite GB was the active nucleus for the pearlite reaction, rather than the ferrite that was proposed in earlier studies [38]. This ensures that all carbides have the same orientation and explains the observed crystallography.

For a low carbon steel, such as a steel containing 0.02% C, pearlite is not formed and, provided the cooling rate is sufficiently slow to prevent C being retained in solution, all the C forms carbides at the ferrite boundaries. Even for a fast cooling rate there is little or no C left in solution at room temperature. Faster cooling rates have the effect of increasing the number carbide nucleation sites, leading to finer carbides. For ferrite-pearlite steels, the carbon source for α/α GB carbides is C in the γ, and subsequent growth is dependent on the C in the ferrite diffusing to the GB and being absorbed by the GB carbides. The amount of C available for precipitation in the form of GB carbides can be thought to correspond to the solubility of C in ferrite at the time of the pearlite reaction. Faster cooling rates will suppress the pearlite transformation to lower temperature and hence the amount of C available for precipitation is reduced, resulting in finer carbides.

Our TEM/STEM observations for X65 pipeline steel did reveal the one case of Fig. 4b where there was carbide at the α/α GB and carbide between the α and pearlite. The volume of material sampled in TEM specimens is extremely small and consequently, sample examination with scanning electron-microcopy and optical microscopy is needed to determine the frequency of occurance of phenomena such as illustrated in Fig. 4b. Such work is presently underway [43] and has identified other examples. This indicates that the example of Fig. 4b does indeed illustrate a new mechanism of pearlite nucleation which is a combination of the models of Mintz *et al.* and Ming. The new model is illustrated in Fig. 4c. A carbide GBC_f precipitates at the α/α GB during the transformation from γ to α, i.e. during the formation of proeutectoid ferrite from the austenite. During this process, carbon is rejected from the ferrite, and accumulates at the α/γ interface. When this carbon concentration reaches a critical value, carbide precipiates at the α/γ interface as suggested by Ming *et al.* Furthermore, Fig. 4c suggested that the carbide at the α/γ interface is nucleated by the carbide GBC_f at the $\alpha:\alpha$ GB. Subsequently, the IB carbide IBC_{fp}, nucleates the pearlite as for the model of Ming *et al.*

4.3. Mn distribution

The addition of Mn was reported to decrease the amount of carbon in solution in α-iron [39, 40] due to a partition of Mn from the ferrite to the carbide. Recently Mn diffusion was suggested to be a potential rate determining factor for the initial ferrite growth for A36 plain carbon steel with 0.74% Mn [41]. Militer *et al.* [41] suggested that the equilibrium concentration of Mn in ferrite was lower than that in austenite, that Mn diffusion in austenite was a relatively slow process so that Mn segregated at the interface between pro-eutectoid ferrite and austenite thereby limiting the mobility of the α/γ boundary. Mintz reported that Mn has also been shown to slow down the diffusion of C and result in a decrease in the transformation temperature so that the amount of carbon diffusing to the GBs may be much less at the higher Mn levels, leading to finer carbides.

The 1.36% Mn concentration in X65 pipeline steel is in the high Mn region according to Mintz's work. For high Mn steels, the GB precipitate growth can be very slow and the GB carbides can be very fine [42]. This leads to the expectation that carbides including GB carbides in X65 should be very fine. The Mn profile shown in Fig. 8 indicated that Mn segregated slightly at α/α GBs with concentrations ranging from 1.0% to 2.4%. No carbide was observed at these GBs. If Mn diffuses along with C, then it would be expected that there would be carbon segregation at the GB where Mn segregates. However, due to the C contamination on the specimen surface, C concentration could not be quantified.

The Mn concentrations were very close to the bulk values for pro-eutectoid ferrite and for ferrite in pearlite. In contrast the Mn concentration in cementite was about 2.2% (Table II). The Mn concentration in cementite was quantified without carbon because of the carbon contamination, but this neglects the 6.7% carbon in the cementite which introduces much more error for cementite quantification than for 0.02% carbon in ferrite, so the real Mn concentration in cementite should be renormalized to be about 1.87% [25]. The ratio of cementite to ferrite in pearlite was calculated as 1 : 7.6 without consideration of the alloying elements. Then the average of Mn concentration in pearlite is about 1.28%. This indicates that there was no significant difference of Mn concentration between pro-eutectoid ferrite and pearlite.

Mn segregated to α/C_p IBs, and desegregated from α/α_p IBs as shown in Figs. 9 and 10. The Mn profiles indicate that the cementite was Mn rich. The highest measured Mn concentration was at the mid-point of cementite. The pattern of Mn segregation could be explained in terms of diffusion in the process zone ahead of the pearlite during the austenite to pearlite transformation and diffusion in the IBs between the proeutectoid ferrite and pearlite when the transformation was complete [25].

The Mn profile across the IB carbide IBC_{fp}, shown in Fig. 12, was similar to that measured previously for X52 [25, 26]. This suggests that the IB carbide IBC_{fp} grew by an extension of the GB carbide GBC_f in the direction 'd' in Fig. 4c; that is growth along the $\alpha:\gamma$ IB in the direction 'd' rather than from the ferrite GB into the austenite along direction 'b'. Furthermore, Fig. 4b suggested that the pearlitic carbide subsequently grew

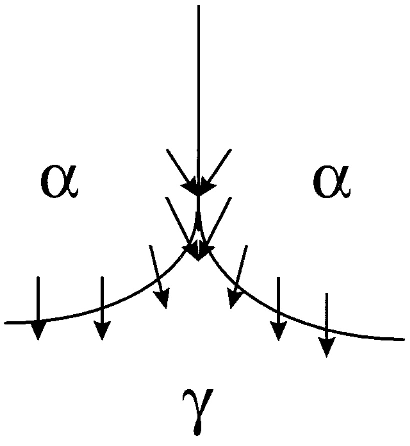

Figure 14 Illustration of carbon diffusion during $\gamma \rightarrow \alpha$ transformation.

from the IB carbide IBC$_{fp}$. Fig. 13 shows that across IBC$_{fp}$ to the point 'A', the Mn profile was the same as that in Fig. 12. At point 'A' the pearlite carbide started, and the Mn content increased along the pearlitic carbide. The pearlitic carbide grew from the side of IB carbide IBC$_{fp}$, from point 'A'. This is quite different to the case where the pearlite meets a clean proeutectoid ferrite GB as shown in Fig. 10. The growth of pearlitic carbide from the IB carbide IBC$_{fp}$ did not result in a high Mn at the interface. As Fig. 13 shows, Mn concentration increased gradually.

These observation reinforce the new mechanism for pearlite formation. GB carbide first forms at a α/α GB, along the lines of the observations and as proposed by Mintz, then grows to the α/γ interface, and finally the pearlite colony initiates at the interface of carbide IBC$_{fp}$ and austenite. Carbon segregates at the triple junction of the growing ferrite grains and austenite, especially at the corner of growing ferrite grain boundaries and austenite as illustrated in Fig. 14. The high carbon content can lead to the formation of the GB carbide GBC$_f$. Also the carbon content is much higher at the interface between ferrite and austenite, so the CB carbide GBC$_f$ grows along the $\alpha:\gamma$ interface and forms the carbide IBC$_{fp}$ which nucleates the pearlite.

5. Conclusions

- There was indeed no segregation at the proeutectoid ferrite GBs of P and S. This indicates that contrary to literature expectations, P and S are not involved in the mechanism of SCC of pipeline steels.
- There was some Mn segregation at the proeutectoid GBs.
- Mn segregated at IB between the cementite and pro-eutectoid ferrite, and desegregated from the IB between pro-eutectoid ferrite and pearlitic ferrite. This patern is attributed to diffusion in the process zone ahead of the pearlite during the austenite to pearlite transformation and diffusion in the IBs between the proeutectoid ferrite and pearlite after the transformation was complete.
- A new mechanism was proposed for pearlite formation. GB carbide first forms at an α/α GB, and then grows along the α/γ interface. Subsequently pearlite initiates from this interface carbide.

Acknowledgement

Authors are grateful to the support by East Australian Pipeline Limited and a University of Queensland External Support Enabling Grant. Thanks for the help of EMU, University of Sydney, especially to Mr Adam Sikorski and Dr Dougal McCulloch. Also thanks to CMM staff at the University of Queensland. Thanks for the helpful discussion with Associate Professor Patrick Kelly.

References

1. A. ATRENS and Z. F. WANG, *J. Mater. Sci.* **33** (1998) 405.
2. A. ATRENS and OEHLERT, *ibid.* **33** (1998) 783.
3. A. OEHLERT and A. ATRENS, *ibid.* **33** (1998) 775.
4. *Idem, ibid.* **32** (1997) 6519.
5. A. ATRENS, Z. F. WANG and J. Q. WANG, *Advances in Fracture Research*, Proceedings of the Ninth International Conference on Fracture, edited by B. L. Karihaloo *et al.* (Pergamon, Oxford, 1997) p. 375.
6. A. OEHLERT and A. ATRENS, *Corrosion Sci.* **38** (1996) 1159.
7. *Idem, Act. Metall. Mater.* **42** (1994) 1493.
8. A. ATRENS and Z. F. WANG, *Mater. Forum* **19** (1995) 9.
9. A. ATRENS, C. C. BROSNAN, S. RAMAMURTHY, A. OEHLERT and I. O. SMITH, *Measurement Sci. Technol.* **4** (1993) 1281.
10. S. RAMAMURTHY and A. ATRENS, *Corrosion Sci.* **34** (1993) 1385.
11. A. ATRENS, R. COADE, J. ALLISON, H. KOHL, G. HOCHORTLER and G. KRIST, *Mater. Forum* **17** (1993) 263.
12. A. S. LIM and A. ATRENS, *Appl. Phys. A* **54** (1992) 270.
13. S. JIN and A. ATRENS, *ibid.* **50** (1990) 287.
14. *Idem, ibid.* **42** (1987) 149.
15. R. M. RIECK, A. ATRENS and I. O. SMITH, *Met. Trans.* **20A** (1989) 889.
16. Federal Power Commission, Bureau of Natural Gas, Washington DC, Final Staff Report on Investigation of Tennessee Gas Transmission Company Pipeline No. 100-1 Failure Near Natchitoches, Louisiana, March 1965.
17. P. J. KENTISH, *Br. Corros. J.* **20** (1985) 139.
18. R. N. PARKINS, Fifth Symposium on Line Pipe Research (American Gas Association Inc, 1974) paper V, U1-40.
19. R. N. PARKINS, E. BELHIMER and W. K. BLANCHARD Jr, *Corrosion* **49** (1993) 951.
20. J. A. BEAVERS, T. K. CHRISTMAN and R. N. PARKINS, *Mater. Performance* (1998) 22.
21. Z. F. WANG and A. ATRENS, *Metall. Mater. Trans.* **27A** (1996) 2686.
22. S. K. BANERJI, C. J. McMAHON and H. C. FENG, *Metall. Trans.* **9A** (1978) 237.
23. R. H. JONES, S. M. BRUEMMER, M. T. JONES and D. C. BAER, *Scripta Metall.* **16** (1982) 615.
24. J. SKOGSMO and A. ATRENS, *Acta Metall.* **42** (1994) 1139.
25. J. Q. WANG, D. R. COUSENS, C. NOCKOLDS and A. ATRENS, *Mater.* **46** (1998) 5677.
26. *Idem*, Corrosion & Prevention 97, 1997.
27. F. C. HULL and R. F. MEHL, *Trans. ASM* **30** (1942) 381.
28. R. F. MEHL and W. C. HAGEL, *Prog. Met. Phys.* **6** (1956) 74.
29. J. W. CAHN and W. C. HAGEL, in "Decomposition of Austenite by Diffusional Processes," edited by W. Z. Zazkay and A. Aaronson (Interscience, New York, 1962) p. 131.
30. B. MINTZ and P. CAMPBELL, *Mater. Sci. Technol.* **5** (1989) 155.
31. B. MINTZ, S. TAJIK and R. VIPOND, *idib.* **10** (1994) 89.
32. M. X. ZHANG, Crystallography of phase transformations in steels, Ph.D. thesis, University of Queensland, 1997, p. 135.
33. M. X. ZHANG and P. M. KELLY, *Met. Trans.*, submitted.
34. J. G. WILLIAMS, C. R. KILLMORE, F. F. J. BARBARO, J. PIPER and L. FLETCHER, *Mater. Forum* **20** (1996) 13.
35. J. P. BENEDICT, R. ANDERSON, S. J. KLEPEIS and M. CHAKER, *Mater. Res. Soc. Symp. Proc.* **199** (1990) 189.
36. P. M. KELLY, A. JOSTSONS, R. G. BLAKE and J. G. NAPIER, *Phys. Stat. Sol. (a)* **81** (1975) 771.
37. G. CLIFF and G. W. LORIMER, *J. Microsc.* **103** (1975) 203.

38. M. HILLERT, "Decomposition of Austenite by Diffusional Processer," edited by V. F. Zacky and H. I. Aaronson (Interscience, New York, 1962) p. 197.
39. P. M. ROBINSON and P. N. RICHARDS, *J. Iron Steel Inst.* (1965) 621.
40. H. BORCHERS and W. KOENIG, *Arch. Eisenh.* **34** (1963) 453.
41. M. MILITZER, R. PANDI and E. B. HAWBOLT, *Metall. Trans. A* **27A** (1996) 1547.
42. H. O. K. KIRCHNER, *Metall. Trans.* **2** (1971) 2861.
43. J. Q. WANG, A. ATRENS, N. N. KINAEV and D. R. COUSENS, *J. Mater. Sci.* **33** (1998) 1.
44. H. MAZILLE and H. H. UHLIG, *Corrosion* **28** (1972) 427.

Received 1 June
and accepted 1 October 1998